# Bayesian Analysis of the Complex Singlet Model with Phase Transition Gravitational Waves

## Qingyuan Liang<sup>a</sup> Ligong Bian<sup>b</sup> Huai-Ke Guo<sup>a</sup> Yongcheng Wu<sup>c,d</sup>

- <sup>a</sup>International Centre for Theoretical Physics Asia-Pacific, University of Chinese Academy of Sciences, Beijing 100190, China
- <sup>b</sup>Department of Physics and Chongqing Key Laboratory for Strongly Coupled Physics, Chongqing University, Chongqing 401331, P. R. China
- <sup>c</sup>Department of Physics, Institute of Theoretical Physics and Institute of Physics Frontiers and Interdisciplinary Sciences, Nanjing Normal University, Nanjing, 210023, China
- <sup>d</sup>Nanjing Key Laboratory of Particle Physics and Astrophysics, Nanjing, 210023, China E-mail: qingyuan211045@gmail.com, lgbycl@cqu.edu.cn, quohuaike@ucas.ac.cn, ycwu@njnu.edu.cn

ABSTRACT: We explore the prospects of probing the Complex Singlet Extension of the Standard Model (CxSM) with gravitational waves from the Electroweak phase transition. The study establishes a connection of the scalar potential parameters, the thermodynamic properties of the phase transition, with the directly measured stochastic gravitational-wave background in the presence of astrophysical background and foreground. Considering the space-based gravitational wave detector Taiji, we construct a frequency-domain likelihood that incorporates instrumental and astrophysical noises, and perform both Fishermatrix forecasts and Bayesian Nested Sampling analysis. The comparison of these two approaches demonstrates consistent parameter recovery and highlights the sensitivity of Taiji to millihertz gravitational-wave signals. We further propagate the inferred constraints on the gravitational-wave spectrum back to the underlying CxSM parameters, obtaining meaningful limits on the Higgs self-couplings. The results emphasize the complementarity between gravitational-wave observations and collider measurements, showing that future missions such as Taiji can serve as a powerful probe of electroweak-scale new physics and the dynamical origin of the Higgs sector.

C	ontents						
1	Introduction						
2	Complex S	Complex Singlet Extension of the Standard Model					
3	The Taiji l	Detector and Data Analysis Framework	5				
	3.1 Grav	itational Waves in Space-Based Detectors	5				
	3.2 Likel	ihood Function and Fisher Information Matrix	7				
4	Parameter Estimation and Phenomenological Studies						
	4.1 Meas	urements of GW Spectrum Parameters	8				
	4.2 Meas	urements of Model Parameters and Higgs Self-Couplings	11				

14

## 1 Introduction

Conclusion

The stochastic gravitational-wave background (SGWB) encodes relic information from the earliest stages of the Universe and provides a unique avenue for probing fundamental physics beyond the reach of colliders [1, 2]. Evidence for such a background has recently been reported in the nanohertz band by pulsar timing array (PTA) collaborations [3–6]. At higher frequencies, ground-based detectors such as Advanced LIGO [7], Virgo [8], and KAGRA [9] have constrained the SGWB up to the kilohertz regime [10]. In the coming decade, space-based interferometers, including LISA [11–13], Taiji [14–16], and TianQin [17–19], are expected to open an observational window in the millihertz band, enabling tests of a wide range of cosmological processes.

Among the potential cosmological sources, first-order phase transitions (FOPTs) are of particular interest [20–25]. The violent bubble expansion and collision during such transitions can generate a stochastic gravitational wave (GW) signal through sound waves (SW) and plasma turbulence. A strongly first-order electroweak phase transition (EWPT) can simultaneously satisfy the out-of-equilibrium condition required for electroweak baryogenesis [26] and yield a potentially detectable GW signal in the frequency range accessible to future space missions [20].

The extraction of a faint cosmological signal from experimental data is, however, complicated by instrumental noise and astrophysical confusion foregrounds [27, 28]. Space-based interferometers rely on time-delay interferometry (TDI) [29] to suppress laser frequency fluctuations, forming three orthogonal data combinations, commonly labeled as

A, E, and T [30]. The so-called null channel T [31] is nearly insensitive to GWs at low frequencies, serving as an internal reference for calibration and noise validation. Foregrounds originating from unresolved compact binaries, both Galactic and extragalactic, constitute an additional stochastic background [32–34], which must be carefully modeled and marginalized in any realistic analysis.

Recent developments have emphasized the importance of combining theoretical modeling with statistically rigorous data analysis [34–39]. Following this direction, we construct a frequency-domain framework for parameter inference that incorporates realistic noise spectra, astrophysical foregrounds, and the detector response of a Taiji-like mission. Both the Fisher information matrix (FIM) forecasts and full Bayesian analysis are performed to evaluate the reconstruction accuracy of the SGWB parameters and to map these spectral constraints onto the underlying particle-physics parameters. Compared with our previous study [40], the present work further accounts for the astrophysical foreground, which significantly affects the detectability of the cosmological background and provides a more realistic assessment. In addition, we employ the nested sampling (NS) algorithm implemented in bilby.dynesty [41] instead of PyMC, enabling GPU acceleration [42] and providing direct estimates of the Bayes factor (BF) for model comparison.

The interplay between collider measurements and GW observations has emerged as a promising frontier for probing the structure of the Higgs potential [43]. In particular, the cubic and quartic Higgs self-couplings, which remain challenging to measure directly at colliders [44, 45], can be indirectly constrained through GWs produced during the EWPT [46]. Building upon our previous work [47], we further investigate the complex singlet extension of the Standard Model (CxSM) [48, 49], aiming to provide deeper insights into the connection between GW observations and particle-physics phenomenology [50]. The model capitalizes on the multi-step phase transition that provides the chance to address dark matter and baryogenesis simultaneously [51, 52].

Using simulated data for a Taiji-like interferometer, we evaluate the detectability of the phase-transition—induced GW spectrum, quantify the expected parameter precision, and propagate the inferred uncertainties to the CxSM scalar potential parameters. The resulting bounds [53] on the Higgs self-couplings demonstrate the complementarity between GW and collider probes of the electroweak symmetry-breaking mechanism.

The remainder of this paper is organized as follows. Sec. 2 introduces the CxSM framework and its scalar potential. Sec. 3 presents the Taiji detector response and the statistical analysis pipeline. Sec. 4 details the parameter estimation results and their implications for the underlying particle physics model. Conclusions are presented in Sec. 5.

## 2 Complex Singlet Extension of the Standard Model

In this work, we consider the SM extended by a complex scalar singlet  $\mathbb{S}$  as a benchmark scenario. The most general scalar potential for such an extension is given as [48, 53]

$$V(\Phi, \mathbb{S}) = \mu^{2} |\Phi|^{2} + \lambda |\Phi|^{4} + \frac{\delta_{2}}{2} |\Phi|^{2} |\mathbb{S}|^{2} + \frac{b_{2}}{2} |\mathbb{S}|^{2} + \frac{d_{2}}{4} |\mathbb{S}|^{4}$$

$$+ \left( \frac{\delta_{1}}{4} |\Phi|^{2} \mathbb{S} + \frac{\delta_{3}}{4} |\Phi|^{2} \mathbb{S}^{2} + c.c. \right)$$

$$+ \left( a_{1} \mathbb{S} + \frac{b_{1}}{4} \mathbb{S}^{2} + \frac{c_{1}}{6} \mathbb{S}^{3} + \frac{c_{2}}{6} \mathbb{S} |\mathbb{S}|^{2} + \frac{d_{1}}{8} \mathbb{S}^{4} + \frac{d_{3}}{8} \mathbb{S}^{2} |\mathbb{S}|^{2} + c.c. \right), \quad (2.1)$$

where  $\Phi$  is the SM scalar doublet. The parameters in the first line of the potential are real, while the parameters in the second and third lines are generally complex. There are two possible global symmetries that can be imposed on the potential: (i) a discrete  $\mathbb{Z}_2$  symmetry under which  $\mathbb{S} \to -\mathbb{S}$  can be imposed to eliminate all terms with odd powers of  $\mathbb{S}$ , e.g.,  $\delta_1, a_1, c_{1,2}$ ; (ii) a global U(1) symmetry under which  $\mathbb{S} \to e^{i\alpha}\mathbb{S}$  eliminates all terms with complex coefficients, e.g.,  $\delta_{1,3}, a_1, b_1, c_{1,2}, d_{1,3}$ . In the current study, we consider the case where  $\mathbb{S}$  acquires a non-zero vev at zero temperature. As a consequence, the real component of  $\mathbb{S}$  mixes with the SM Higgs. U(1) and  $\mathbb{Z}_2$  symmetries are both spontaneously broken by the singlet vev, and the Goldstone boson corresponding to the single  $\mathbb{S}$  is stable but massless. An U(1) symmetry breaking term is required to generate a corresponding mass, for which the  $b_1$  term is used. On the other hand, the spontaneously broken  $\mathbb{Z}_2$  symmetry will lead to the cosmological domain wall problem [54, 55]. To avoid this, we further introduce a soft  $\mathbb{Z}_2$  breaking term  $(a_1)$ . Then, the potential we considered for the following study reads [48]:

$$V(\Phi, \mathbb{S}) = \mu^{2} |\Phi|^{2} + \lambda |\Phi|^{4} + \frac{\delta_{2}}{2} |\Phi|^{2} |\mathbb{S}|^{2} + \frac{b_{2}}{2} |\mathbb{S}|^{2} + \frac{d_{2}}{4} |\mathbb{S}|^{4} + \left(a_{1} \mathbb{S} + \frac{b_{1}}{4} \mathbb{S}^{2} + c.c.\right).$$
(2.2)

Note that this is not a unique choice for the potential purpose discussed above.

To minimize the scalar potential, we expand the scalar around the vevs as

$$\Phi = \begin{pmatrix} 0 \\ \frac{v+\phi}{\sqrt{2}} \end{pmatrix}, \quad \mathbb{S} = \frac{v_s + \eta + iA}{\sqrt{2}}, \tag{2.3}$$

where we have suppressed the Goldstone boson. The vevs are determined by the corresponding minimization conditions as

$$\begin{cases}
0 = \frac{\partial V}{\partial v} = \mu^2 v + \lambda v^3 + \frac{\delta_2}{4} v v_s^2, \\
0 = \frac{\partial V}{\partial v_s} = \frac{\delta_2}{4} v^2 v_s + \sqrt{2} a_1 + \frac{b_1 + b_2}{2} v_s + \frac{d_2}{4} v_s^3
\end{cases} ,$$
(2.4)

thus

$$\begin{cases} \mu^2 = -\lambda v^2 - \frac{\delta_2}{4} v_s^2, \\ b_1 + b_2 = -2\sqrt{2} \frac{a_1}{v_s} - \frac{\delta_2}{2} v^2 - \frac{d_2}{2} v_s^2 \end{cases}$$
 (2.5)

The mass spectrum of the scalars can be obtained after inserting the above relationships as follows:

$$m_A^2 = -b_1 - \sqrt{2} \frac{a_1}{v_s},\tag{2.6}$$

$$\mathcal{M}_{\phi\eta}^2 = \begin{pmatrix} \mu_{\phi}^2 & \mu_{\phi\eta}^2 \\ \mu_{\phi\eta}^2 & \mu_{\eta}^2 \end{pmatrix},\tag{2.7}$$

$$\mu_{\phi}^2 = 2\lambda v^2,\tag{2.8}$$

$$\mu_{\eta}^2 = \frac{d_2}{2}v_s^2 - \sqrt{2}\frac{a_1}{v_s},\tag{2.9}$$

$$\mu_{\phi\eta}^2 = \frac{\delta_2}{2} v v_s. \tag{2.10}$$

The scalars  $\phi$  and  $\eta$  therefore mix according to

$$\begin{pmatrix} h \\ s \end{pmatrix} = \begin{pmatrix} c_{\theta} & s_{\theta} \\ -s_{\theta} & c_{\theta} \end{pmatrix} \begin{pmatrix} \phi \\ \eta \end{pmatrix}, \tag{2.11}$$

which diagonalizes the mass matrix with the corresponding masses  $m_h$ ,  $m_s$ , and  $c_\theta \equiv \cos \theta$ ,  $s_\theta \equiv \sin \theta$ . In terms of the masses  $(m_h, m_s, m_A)$ , vevs  $(v, v_s)$  and the mixing angle  $\theta$ , quartic couplings can be expressed as

$$\lambda = \frac{1}{2v^2} \left( c_{\theta}^2 m_h^2 + s_{\theta}^2 m_s^2 \right), \tag{2.12}$$

$$d_2 = \frac{2}{v_s^2} \left( s_\theta^2 m_h^2 + c_\theta^2 m_s^2 + \sqrt{2} \frac{a_1}{v_s} \right), \tag{2.13}$$

$$\delta_2 = \frac{2}{vv_s} \left( m_h^2 - m_s^2 \right) s_\theta c_\theta. \tag{2.14}$$

Then the input parameters are given as

$$v(= 246 \,\text{GeV}), v_s, m_h(= 125 \,\text{GeV}), m_s, m_A, \theta, a_1.$$
 (2.15)

In the following studies, we scan these parameters within the specified ranges:

$$v_s \in [0, 150] \text{ GeV}, m_s \in [65, 150] \text{ GeV}, m_A \in [65, 2000] \text{ GeV},$$
  
 $\theta \in [0, 0.5], \sqrt[3]{a_1} \in [-100, 100] \text{ GeV}$  (2.16)

It is worth noting that the electroweak phase transition may occur through either a onestep or a two-step route. However, only a negligible subset of the scanned parameter space exhibits the two-step pattern. For this reason, our analysis focuses exclusively on the onestep transition points. With the above setup for the model parameters, we define the deviations of the cubic and quartic self-couplings of the SM-like Higgs as [53]

$$\delta\kappa_{3} \equiv \frac{\lambda_{hhh}}{\lambda_{hhh}^{SM}} - 1 = c_{\theta}^{3} - 1 + \frac{v}{v_{s}} s_{\theta}^{3} + \sqrt{2} \frac{v}{v_{s}} \frac{a_{1}}{m_{h}^{2} v_{s}} s_{\theta}^{3}, \qquad (2.17)$$

$$\delta\kappa_{4} \equiv \frac{\lambda_{hhh}}{\lambda_{hhh}^{SM}} - 1 = c_{\theta}^{6} - 1 + \frac{v^{2}}{v_{s}^{2}} s_{\theta}^{6} + \frac{v^{2}}{v_{s}^{2}} \frac{m_{s}^{2}}{m_{h}^{2}} s_{\theta}^{4} c_{\theta}^{2} + 2 \frac{v}{v_{s}} \frac{m_{h}^{2} - m_{s}^{2}}{m_{h}^{2}} s_{\theta}^{3} c_{\theta}^{3} + \frac{m_{s}^{2}}{m_{h}^{2}} s_{\theta}^{2} c_{\theta}^{4} + \sqrt{2} \frac{v^{2}}{v_{s}^{2}} \frac{a_{1}}{m_{h}^{2} v_{s}} s_{\theta}^{4}. \qquad (2.18)$$

## 3 The Taiji Detector and Data Analysis Framework

Taiji is a proposed space-based GW observatory designed to probe the millihertz frequency band, where a rich variety of astrophysical and cosmological sources are expected to exist. Its triangular constellation, consisting of three drag-free spacecraft in heliocentric orbits, provides multiple long-baseline interferometric measurements that enable high-sensitivity detection of signals such as the SGWB generated by an EWPT. Notably, the predicted peak frequency of the EWPT-induced SGWB typically falls within the optimal sensitivity range of space-based detectors, such as LISA and Taiji.

This section presents an overview of the Taiji mission concept and its interferometric measurement strategy. We describe the TDI technique [32], which suppresses the otherwise overwhelming laser frequency noise and yields the orthogonal A, E, and T data channels used for scientific analysis. We then summarize the frequency-domain statistical framework [34] employed in SGWB searches, including the modeling of the detector response functions, instrumental noise spectra, and channel correlations, following the conventions established in [40]. Finally, we introduce the likelihood function and the FIM formalism that we use to forecast the constraints on the parameters characterizing the GW spectrum and the underlying particle-physics model.

#### 3.1 Gravitational Waves in Space-Based Detectors

Taiji employs a triangular constellation of three spacecraft, labeled A, B, and C, separated by arm lengths of  $L=3\times 10^9\,\mathrm{m}$  (and  $L=2.5\times 10^9\,\mathrm{m}$  for LISA) [14–16]. Each spacecraft exchanges laser beams with the other two, forming three unequal-arm Michelson interferometers. The resulting frequency-domain data streams  $\tilde{d}_i(f)$  (i=1,2,3) are linearly recombined into the orthogonal TDI channels  $\tilde{d}_I(f)$  (I=A,E,T), following the same setup as in [40].

The single-sided PSD of each TDI channel is written as

$$P_a(f) = S_a(f) + N_a(f), \qquad a \in \{A, E, T\},$$
 (3.1)

where  $S_a(f)$  and  $N_a(f)$  denote the GW signal and instrumental noise contributions. The signal component is related to the GW energy density spectrum via

$$S_a(f) = \frac{3H_0^2}{4\pi^2} \frac{\Omega_{\text{GW}}(f)}{f^3} \mathcal{R}_a(f),$$
 (3.2)

where  $\mathcal{R}_a(f)$  is the detector response. The explicit forms of  $\mathcal{R}_a(f)$  and  $N_a(f)$  are given in [40]. We adopt the nominal noise parameters

$$N_{\rm acc} = 3 \times 10^{-15}, \qquad \delta x = 8 \times 10^{-12},$$

and  $\delta x = 15 \times 10^{-12}$  for LISA.

Following [56], the sensitivity function of each TDI channel is defined as

$$S_I(f) = \sqrt{\frac{N_I(f)}{\mathcal{R}_I(f)}}, \qquad I = A, E, T.$$
(3.3)

The corresponding SNR is

$$SNR_I = \sqrt{2T_t \int_0^\infty \left(\frac{S_I(f)}{N_I(f)}\right)^2 df}, \qquad I = A, E, T,$$
(3.4)

where  $T_t$  is the total observation time specified in the next section.

Since the null-channel method assumes that the T channel is free of signals, only the A/E channel is employed for evaluating sensitivity and SNR. The resulting sensitivity curves for LISA and Taiji are shown in Fig. 1. The solid curves correspond to the model-based sensitivities obtained from Eq. (3.3).

In this work, we consider a mixed scenario in which the cosmological signal is superimposed on a stochastic astrophysical foreground and background. To mitigate the parameter degeneracies highlighted in [34, 40], we restrict our attention to two geometric parameters that characterize the SW contribution: the peak amplitude  $\Omega_0$  and the peak frequency  $f_p$ .

The total GW energy density spectrum is modeled as the sum of three components—the galactic foreground, the astrophysical background, and the SW contribution:

$$\Omega_{\rm GW}(f) = \Omega_{\rm dwd}(f) + \Omega_{\rm GW,ast}(f) + \Omega_{\rm sw}(f). \tag{3.5}$$

The galactic foreground, dominated by unresolved double white-dwarf (DWD) binaries, is modeled by a broken power law [57],

$$\Omega_{\text{dwd}}(f) = \frac{A_1 \left( f/f_* \right)^{\alpha_1}}{1 + A_2 \left( f/f_* \right)^{\alpha_2}},\tag{3.6}$$

where  $f_*$  is the characteristic frequency defined as  $f_* = \frac{c}{2\pi L}$ . The astrophysical background is parameterized by a single power law [27],

$$\Omega_{\rm GW,ast}(f) = \Omega_{\rm ast} \left(\frac{f}{f_{\rm ref}}\right)^{\varepsilon},$$
(3.7)

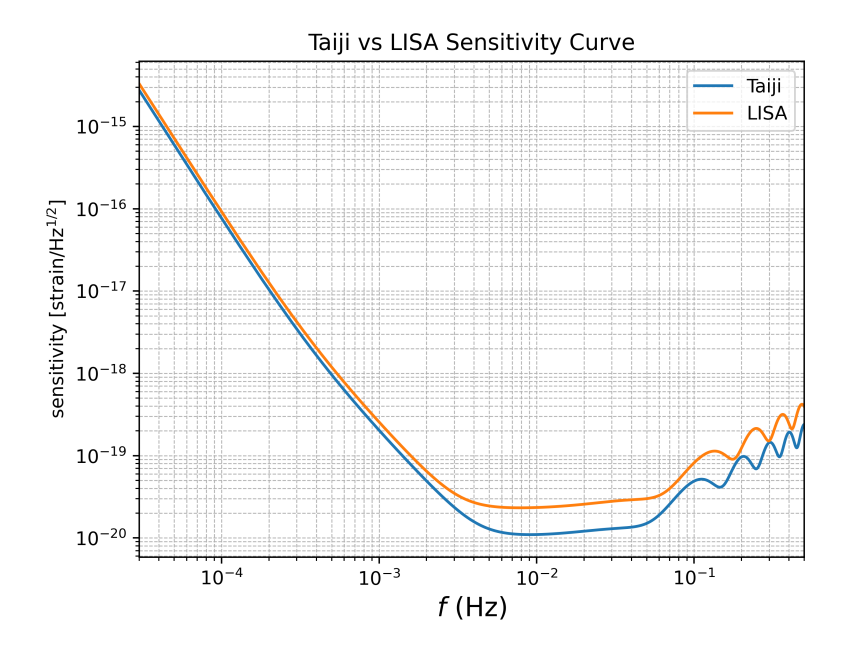


**Figure 1**. Sensitivity curves for LISA and Taiji. Solid lines correspond to the model-based results from Eq. (3.3).

where  $\Omega_{\rm ast}$  is the amplitude at the reference frequency  $f_{\rm ref}=1~{\rm mHz}$ , and  $\varepsilon$  is the spectral index.

The SW component, corresponding to the acoustic contribution from a FOPT, is modeled by a broken power-law template [40, 46]:

$$\Omega_{\rm sw}(f) = \Omega_0 \left(\frac{f}{f_{\rm p}}\right)^3 \left[\frac{7}{4 + 3(f/f_{\rm p})^2}\right]^{7/2}.$$
(3.8)

In this study, we focus on assessing the detectability of the cosmological background. Accordingly, the SNR and BF quantify both the strength of the signal and its likelihood of being distinguished from the underlying noise. To characterize the SNR, we consider two definitions. The absolute SNR ( $SNR_a$ ) compares the cosmological background solely against the instrumental noise, providing a measure of its intrinsic amplitude. In contrast, the relative SNR ( $SNR_r$ ) incorporates the astrophysical foreground and background into the effective noise budget. This quantity is more relevant for realistic data analysis, as it reflects the observational challenges posed by astrophysical contamination. Moreover,  $SNR_r$  is directly aligned with the interpretation of the BF: both compare a "signal + noise" model against a "noise-only" model that already includes all astrophysical components, enabling a meaningful and consistent assessment of detectability across different metrics.

#### 3.2 Likelihood Function and Fisher Information Matrix

During the operation of space-based detectors, interruptions and data gaps divide the observation period into  $N_0$  valid time segments of duration T, yielding a total observing time

of  $T_t = N_0 T$ . In this work, we take  $T = 10^6$  s and  $N_0 = 126$ , corresponding to an effective duration of approximately four years. The data are sampled at a rate  $f_s = 1/\Delta t$ , which satisfies  $f_s > 2f_{\rm max}$  according to the Nyquist criterion, where  $f_{\rm max}$  denotes the highest frequency of interest. The corresponding frequency resolution is  $\Delta f = 1/T$ . For convenience, we set  $\Delta t = 1$  s, leading to a frequency range of  $[3 \times 10^{-5}, 0.5]$  Hz. These conventions are consistent with our previous analysis [40] and with the LISA study [34].

For the statistical inference, we adopt the same likelihood and FIM formulations as in [40]. The log-likelihood function is given by

$$\ln \mathcal{L} = -\sum_{\kappa=1}^{N_0} \sum_{k=1}^{N/2} \left\{ \ln \left[ \frac{\pi^3 T^3 f_s^6 (S_A + N_A) (S_E + N_E) N_T}{8} \right] + \frac{2}{T f_s^2} \left[ \frac{|\tilde{d}_A^{\kappa}(f_k)|^2}{S_A(f_k) + N_A(f_k)} + \frac{|\tilde{d}_E^{\kappa}(f_k)|^2}{S_E(f_k) + N_E(f_k)} + \frac{|\tilde{d}_T^{\kappa}(f_k)|^2}{N_T(f_k)} \right] \right\},$$
(3.9)

where  $\tilde{d}_a^{\kappa}(f_k)$  denotes the discrete Fourier transform (DFT) of the a-th TDI channel in the  $\kappa$ -th segment.

The corresponding FIM takes the form

$$F_{ij} = N_0 \sum_{k=1}^{N/2} \left[ \frac{2}{\left(S_A(f_k) + N_A(f_k)\right)^2} \frac{\partial \left(S_A(f_k) + N_A(f_k)\right)}{\partial \theta_i} \frac{\partial \left(S_A(f_k) + N_A(f_k)\right)}{\partial \theta_j} + \frac{1}{N_T^2(f_k)} \frac{\partial N_T(f_k)}{\partial \theta_i} \frac{\partial N_T(f_k)}{\partial \theta_j} \right],$$
(3.10)

where  $\theta_i$  denotes the model parameters.

# 4 Parameter Estimation and Phenomenological Studies

In this section, we investigate how GW observations—particularly from space-based detectors such as Taiji and LISA—can inform BSM particle physics models (see [34, 40] for examples). In particular, we examine how the detection or non-detection of a SGWB constrains the parameter space of models predicting a strong FOPT in the early Universe. By linking the dynamics of the EWPT to its GW signals, we show that GW observations provide an independent and complementary probe to collider and dark matter experiments, offering additional constraints on scenarios such as the CxSM.

### 4.1 Measurements of GW Spectrum Parameters

To assess the detectability of the SW signal sourced by a cosmological FOPT, we employ both Bayesian inference via NS and the FIM approach. These methods offer complementary perspectives: NS reconstructs the full posterior distributions, capturing non-Gaussianity and parameter degeneracies, while the FIM provides a fast, approximate forecast of uncertainties under the Gaussian-likelihood assumption.

Parameter	Injected Value	Recovered Value	Prior (Uniform)	Uncertainty (FIM)	Uncertainty (NS)
$N_{\rm acc}(\times 10^{-15})$	3.00	3.00	(0, 20)	0.13%	0.13%
$\delta x (\times 10^{-12})$	8.00	8.00	(0, 20)	0.008%	0.008%
$\log_{10} A_1$	-15.4	-15.46	(-18, -5)	0.56%	0.54%
$\alpha_1$	-5.7	-5.77	(-15, -3)	1.58%	1.51%
$\log_{10} A_2$	-6.32	-6.37	(-10, 5)	1.10%	1.05%
$\alpha_2$	-6.2	-6.26	(-10, -1)	1.26%	1.19%
$\log_{10}\Omega_{\rm ast}$	-11.0	-11.01	(-15, -8)	0.31%	0.30%
arepsilon	2/3	0.68	(0, 1)	4.58%	4.30%
$\log_{10}\Omega_0$	-11.31	-11.31	(-15, -5)	0.72%	0.72%
$\log_{10} f_{ m p}$	-2.24	-2.25	(-7, -0.1)	1.06%	0.98%

**Table 1**. Fiducial values and uniform prior ranges adopted for data simulation and NS analysis, together with the recovered parameter values and relative uncertainties from both FIM and NS. The SW component yields an absolute SNR of  $\mathrm{SNR}_a \simeq 80$  and a relative SNR of  $\mathrm{SNR}_r \simeq 53$ , discussed at the end of Sec.3.1. The two methods show excellent agreement across all parameters. In several cases, the NS uncertainties appear slightly smaller than those predicted by the FIM; this does not violate the Cramér–Rao bound and is most likely a consequence of statistical fluctuations inherent in the simulated data. A further advantage of NS is that it directly provides the BF; for the SW component we obtain  $\ln \mathrm{BF} = 11.6$ , indicating decisive evidence in favor of the signal model.

We perform NS to derive credible intervals and posteriors for  $(\Omega_0, f_p)$  under various observational setups. In parallel, the FIM is used to estimate the expected sensitivity and to identify possible degeneracies or nonlinear effects that may not be captured by the Gaussian approximation.

Synthetic datasets are generated assuming the fiducial values listed in Table 1. Bayesian parameter estimation is then carried out using NS with uniform priors, chosen to cover realistic ranges following [40, 57]. The inference includes instrumental noise parameters  $(N_{\rm acc}, \delta x)$ , foreground and background parameters  $(A_1, \alpha_1, A_2, \alpha_2, \Omega_{\rm ast}, \varepsilon)$ , and the cosmological signal parameters  $(\Omega_0, f_{\rm p})$ . The resulting posteriors are compared with the confidence ellipses obtained from the FIM.

Fig. 2 shows the NS results: the red contours denote the 68% and 95% credible regions obtained from NS, while the blue ellipses correspond to the FIM predictions. The two approaches exhibit good overall agreement, with small deviations in higher-dimensional projections arising from fluctuations in simulation and sampling, and mild departures from Gaussianity.

The NS analysis, performed using bilby. dynesty, yields the recovered parameter values, associated uncertainties, and the Bayes factor (BF) summarized in Table 1. For the SW component, we obtain  $\ln \mathrm{BF} = 11.6$ , which indicates a strong statistical preference

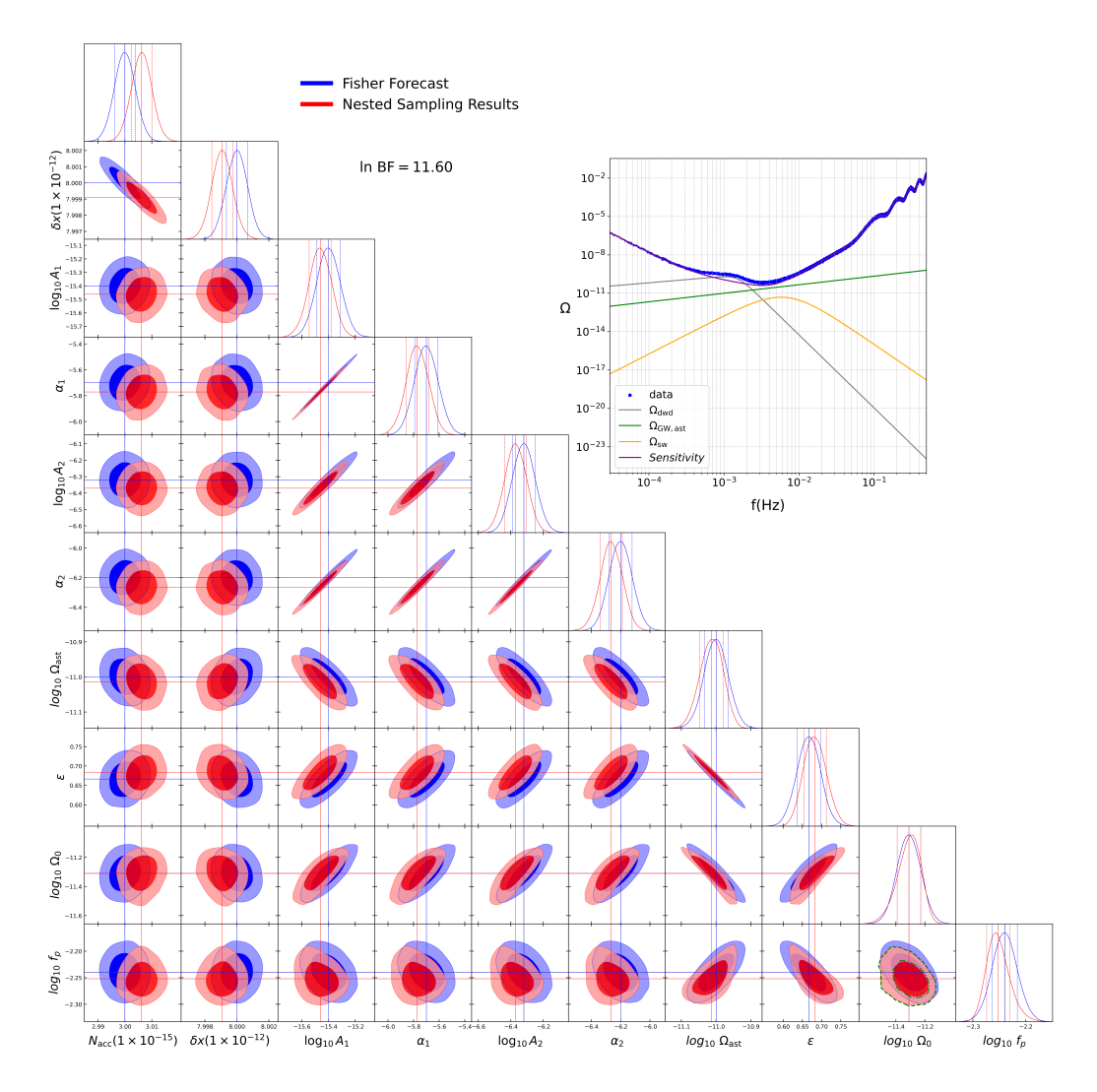
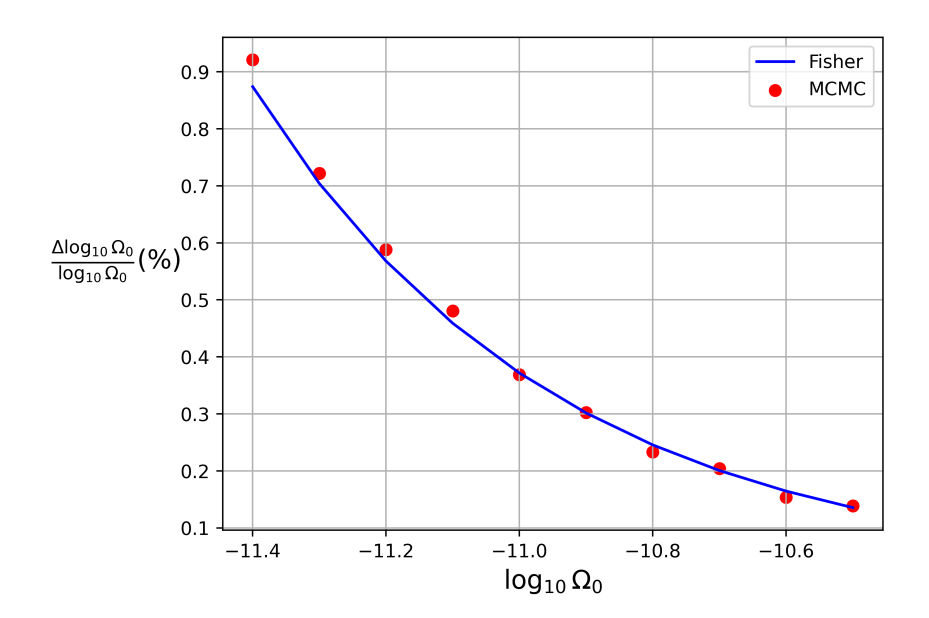


Figure 2. Comparison of parameter constraints obtained from NS (red) and FIM (blue). The dark and light shaded regions denote the 68% and 95% confidence intervals, respectively. The analysis includes two instrumental noise parameters  $(N_{\rm acc}, \delta x)$ , four galactic foreground parameters  $(A_1, \alpha_1, A_2, \alpha_2)$ , two astrophysical background parameters  $(\Omega_{\rm ast}, \varepsilon)$ , and two SW signal parameters  $(\Omega_0, f_{\rm p})$ . The corner plot illustrates that the NS posteriors are in good agreement with the FIM predictions, with mild deviations attributable to fluctuation in sampling and simulation, and weak non-Gaussian effects. The diagonal panels display the one-dimensional marginalized distributions, with dashed vertical lines marking the  $1\sigma$  intervals (blue for FIM, red for NS). The inset figure in the upper-right corner shows the energy-density spectra of the individual components: the galactic foreground  $\Omega_{\rm dwd}$  (gray), the astrophysical background  $\Omega_{\rm GW,ast}(f)$  (green), the SW signal  $\Omega_{\rm sw}(f)$  (orange), and the detector sensitivity curve (purple). The simulated total data points are shown in blue.

for all models that include the SW contribution over the hypothesis without it.

To further illustrate the dependence of parameter precision on the signal amplitude, we perform NS analysis for a sequence of injected  $\Omega_0$  values, compute the corresponding



**Figure 3**. Relative uncertainty on  $\Omega_0$  obtained from NS (red points) compared with the FIM prediction (blue line). As expected, the uncertainty decreases for larger  $\Omega_0$ , reflecting the improvement in parameter precision with increasing SW signal strength.

$\log_{10}\Omega_0$	-11.4	-11.3	-11.2	-11.1	-11.0	-10.9	-10.8	-10.7	-10.6
$SNR_a$	65	82	103	130	163	206	259	326	411
$SNR_r$	43	54	68	86	108	136	171	215	271
ln BF	5	14	22	41	77	124	236	365	583

**Table 2**. SNR values (including both the absolute  $SNR_a$  and the relative  $SNR_\tau$ ; see Sec. 3.1 for definitions) and  $\ln BF$  for different injected  $\Omega_0$  amplitudes. Both quantities increase with signal strength, showing that stronger SW signals not only enhance the detection significance, but also yield greater Bayesian evidence in favor of the signal model.

relative uncertainties, and compare them with the FIM predictions. The results are shown in Fig. 3. We also list the associated SNR and BF values for these injections in Table 2, demonstrating explicitly how both quantities scale with increasing signal strength.

## 4.2 Measurements of Model Parameters and Higgs Self-Couplings

We perform a comprehensive scan over the CxSM parameter space, characterized by five key input parameters, with the benchmark point given by

$$v_s = 23.28 \,\text{GeV}, \, m_s = 62.59 \,\text{GeV}, \, m_A = 1722 \,\text{GeV}, \, \theta = 0.32, \, a_1 = -7.22 \times 10^4 \,(\text{GeV})^3.$$

This benchmark leads to the thermodynamic parameters

$$\frac{\beta}{H_n} = 1098$$
,  $T_n = 17.46 \text{ GeV}$ ,  $\alpha = 6.66$ ,

which together describe a strong FOPT capable of producing an observable GW signal. The geometric parameters  $(\Omega_0, f_{\rm p})$  of the SW component listed in Table 1 are derived directly from these thermodynamic values, yielding an absolute SNR of  ${\rm SNR}_a \simeq 80$  and a relative SNR of  ${\rm SNR}_r \simeq 53$ .

For each sampled point in the CxSM parameter space, we compute the corresponding geometric parameters  $(\Omega_0, f_p)$  that characterize the SW contribution to the GW spectrum. These results are then compared with the confidence regions obtained from both the FIM and NS analysis.

By exploiting the established mapping between the geometric parameters and the CxSM model parameters, we propagate the constraints on  $(\Omega_0, f_p)$  back to the underlying model space. This procedure allows us to identify the regions of the CxSM parameter space that are most compatible with a potential GW detection. The corresponding NS results are presented in Fig. 5.

The posterior distributions obtained from the NS analysis can be directly mapped onto the Higgs self-coupling deviations,  $\delta\kappa_3$  and  $\delta\kappa_4$ , using the relations discussed in Sec. 2. Fig. 6 shows the resulting correlations between these two couplings in the CxSM. Each point corresponds to a viable parameter configuration capable of generating a detectable SGWB signal. Blue points represent the full set of scanned CxSM samples, while red and green points denote the subsets falling within the  $1\sigma$  and  $2\sigma$  confidence regions, respectively, in the spectral parameter plane  $(\log_{10}\Omega_0, \log_{10}f_p)$ . The black filled star marks the benchmark model used for generating the mock signal.

As illustrated in the figure, the inferred distributions exhibit clear correlations between  $\delta \kappa_3$  and  $\delta \kappa_4$ , reflecting how variations in the scalar potential parameters impact the shape and amplitude of the GW spectrum. Because planned experiments have little

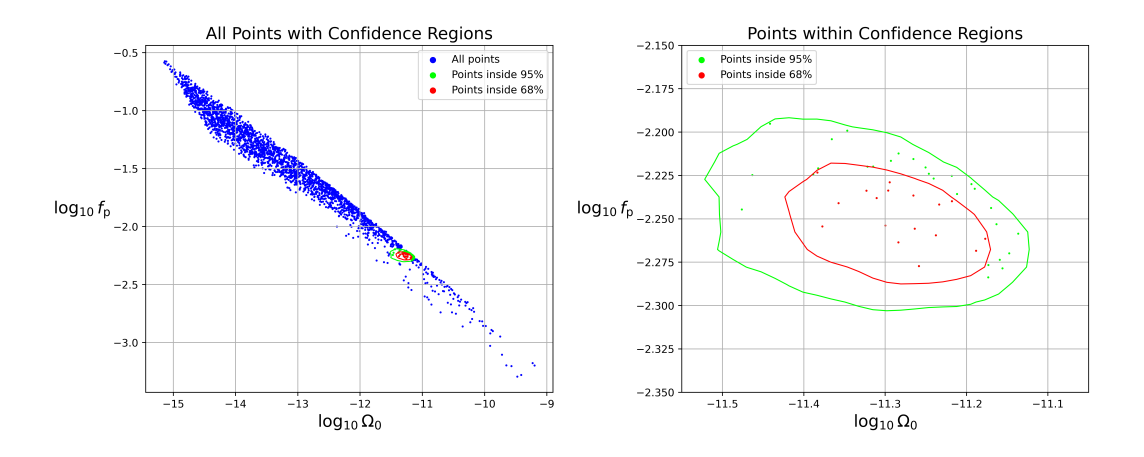
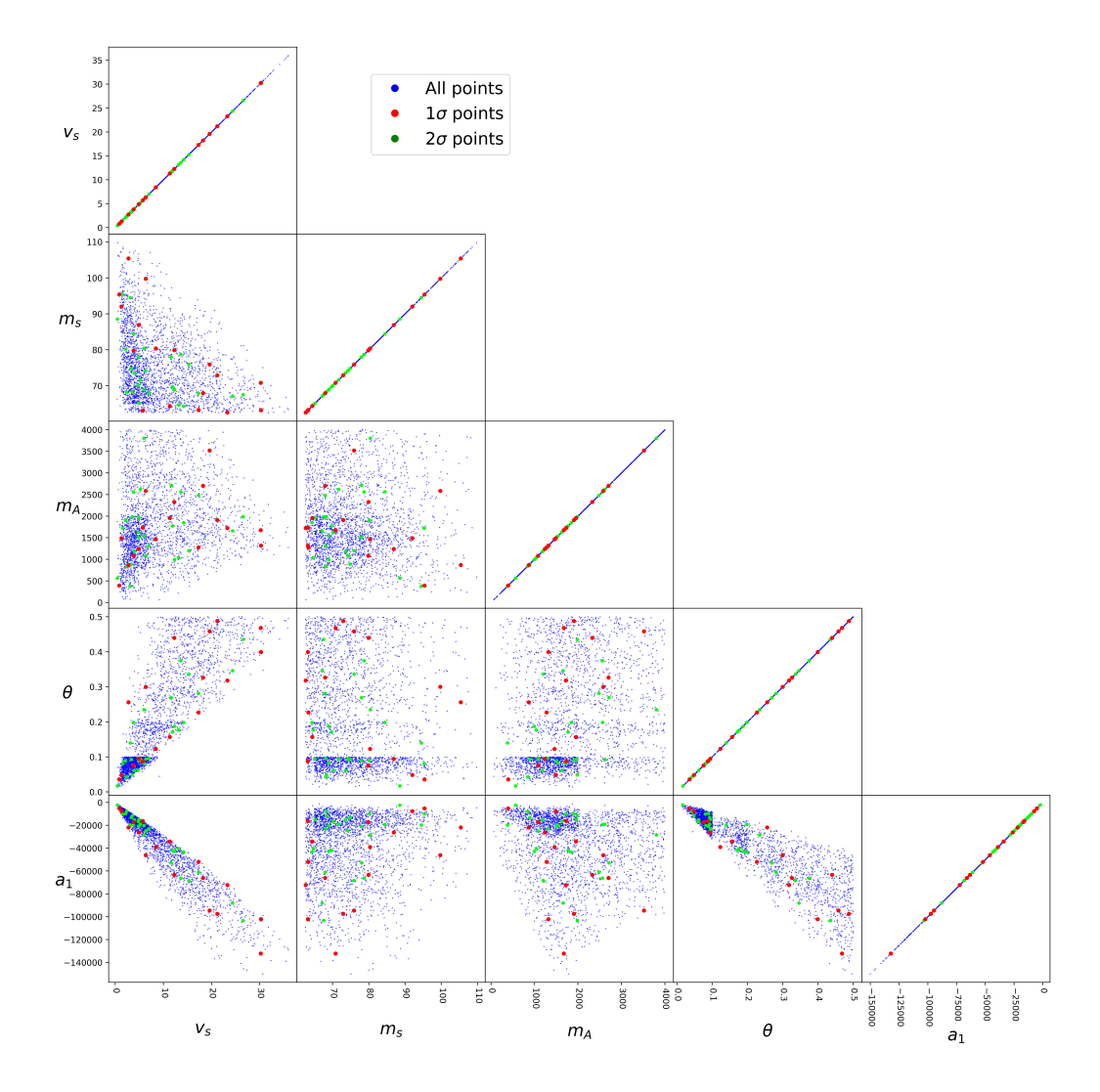


Figure 4. Constraints on the geometric parameters  $\log_{10}\Omega_0$  and  $\log_{10}f_p$  obtained from NS. Blue points represent the full set of parameter combinations from the CxSM scan, while red and green points correspond to those falling within the 68% and 95% confidence regions, respectively. The left panel shows the complete distribution of sampled points, whereas the right panel provides a zoomed-in view highlighting the region favored by the data.



**Figure 5**. Constraints on the CxSM parameters inferred from the NS posterior distributions. Blue points denote the full set of scanned parameter points, while red and green points correspond to those lying within the 68% and 95% credible regions, respectively, as determined from the geometric parameter posteriors. The distributions illustrate how GW observations can significantly narrow the viable regions of the scalar potential parameter space.

sensitivity to the quartic deviation  $\delta \kappa_4$  [58], the vertical placement of the bands in  $\delta \kappa_4$  is purely illustrative and does not reflect any physical constraints. Nevertheless, the noticeable narrowing of the red and green regions compared with the full scan demonstrates that GW-based inference can meaningfully restrict the viable self-interaction structure of the scalar potential, even in parameter directions that remain poorly constrained by collider measurements.

For comparison, the horizontal bars in Fig. 6 indicate the projected 68% and 95% sensitivities to  $\delta\kappa_3$  at future collider facilities, including the HL-LHC, CEPC, ILC, FCC,

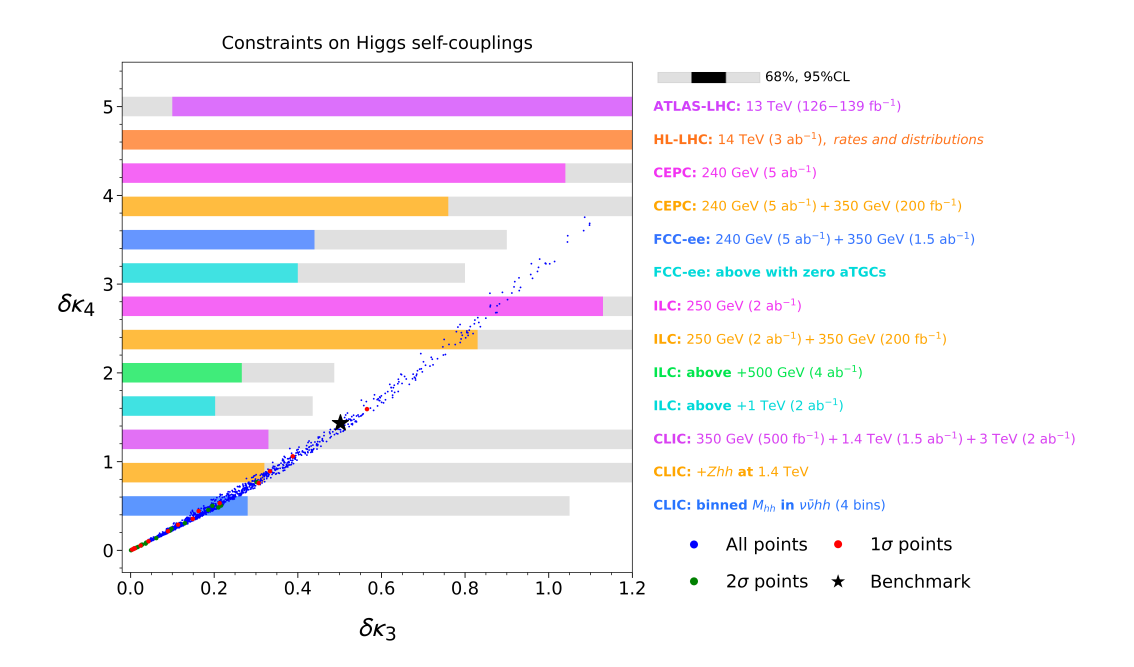


Figure 6. Constraints from GW observations on the Higgs self-coupling deviations,  $\delta \kappa_3$  and  $\delta \kappa_4$ , inferred from the Bayesian analysis of the stochastic GW signal in the CxSM. Each point corresponds to a viable model configuration capable of producing a detectable SGWB spectrum. Blue points denote the full CxSM scan, while red and green points indicate the subsets consistent with the  $1\sigma$  and  $2\sigma$  confidence regions, respectively, in the spectral parameter plane ( $\log_{10}\Omega_0$ ,  $\log_{10}f_p$ ). The black filled star marks the benchmark model used for signal injection. Horizontal bars show the projected 68% and 95% sensitivities to  $\delta \kappa_3$  at future colliders such as the HL-LHC, CEPC, ILC, FCC, and CLIC [44]. This comparison highlights the complementarity between GW inference and collider measurements in probing the scalar potential.

and CLIC [44, 59]. This highlights the strong complementarity between GW observations and collider probes in exploring extended Higgs sectors.

## 5 Conclusion

In this work, we have presented a comprehensive study of cosmological phase transitions and their GW signals within the framework of the CxSM. By linking the scalar potential parameters to the thermodynamic quantities of the FOPT and subsequently to the spectral properties of the resulting SGWB, we have established a self-consistent bridge between particle physics and GW observations.

Using a Taiji-like detector response model, we constructed a frequency-domain likelihood that incorporates instrumental noise, astrophysical foregrounds and backgrounds, and applied both FIM and NS analysis. The two approaches yield consistent results, demonstrating that Taiji possesses the sensitivity required to detect millihertz GWs from strong FOPT and to precisely recover the key spectral parameters ( $\Omega_0$ ,  $f_D$ ).

We further propagated these constraints onto the CxSM parameter space and mapped them to the Higgs self-coupling deviations  $(\delta \kappa_3, \delta \kappa_4)$ . The results show that GW-based inference can place meaningful restrictions on the scalar potential and its self-interaction structure, providing a complementary avenue to collider measurements such as those anticipated at the HL-LHC, CEPC, ILC, FCC, and CLIC.

Overall, this work highlights the strong synergy between future space-based GW detectors and collider experiments in probing electroweak-scale new physics. The methodology developed here offers a general and flexible framework for connecting theoretical models of phase transitions with realistic GW data analysis, paving the way toward a deeper understanding of the Higgs sector through multi-messenger cosmology.

# Acknowledgements

We would like to thank Ju Chen, Ming-Hui Du, Chang Liu for helpful discussions. This work is supported by the startup fund provided by the University of Chinese Academy of Sciences and by the National Science Foundation of China (NSFC) under Grant No. 12147103 and No. 12475109. L.B. is supported by the National Natural Science Foundation of China (NSFC) under Grants Nos. 12347101, 12322505, 12075041. L.B. also acknowledges the Chongqing Natural Science Foundation under Grant No. CSTB2024NSCQ-JQX0022 and Chongqing Talents: Exceptional Young Talents Project No. cstc2024ycjh-bgzxm0020. Y.Wu is supported by NSFC under Grant No. 12305112.

## References

- [1] R. Caldwell et al., *Detection of early-universe gravitational-wave signatures and fundamental physics*, *Gen. Rel. Grav.* **54** (2022) 156 [2203.07972].
- [2] B. LiGong, P. Shi and S.-J. Wang, *Gravitational waves originated from the early universe:* A review and perspective, Sci. Sin. Phys. Mech. Astro. **55** (2025) 230405.
- [3] NANOGRAV collaboration, *The NANOGrav 15 yr Data Set: Evidence for a Gravitational-wave Background*, *Astrophys. J. Lett.* **951** (2023) L8 [2306.16213].
- [4] NANOGRAV collaboration, *The NANOGrav 15 yr Data Set: Observations and Timing of 68 Millisecond Pulsars*, *Astrophys. J. Lett.* **951** (2023) L9 [2306.16217].
- [5] EPTA collaboration, *The second data release from the European Pulsar Timing Array I. The dataset and timing analysis*, *Astron. Astrophys.* **678** (2023) A48 [2306.16224].
- [6] P. Athron, A. Fowlie, C.-T. Lu, L. Morris, L. Wu, Y. Wu et al., *Can Supercooled Phase Transitions Explain the Gravitational Wave Background Observed by Pulsar Timing Arrays?*, *Phys. Rev. Lett.* **132** (2024) 221001 [2306.17239].
- [7] LIGO SCIENTIFIC, VIRGO collaboration, All-sky search for long-duration gravitational wave transients in the first Advanced LIGO observing run, Class. Quant. Grav. 35 (2018) 065009 [1711.06843].

- [8] P. Kumar and T. Dent, *Optimized search for a binary black hole merger population in LIGO-Virgo O3 data*, *Phys. Rev. D* **110** (2024) 043036 [2403.10439].
- [9] KAGRA collaboration, *Overview of KAGRA: Detector design and construction history*, *PTEP* **2021** (2021) 05A101 [2005.05574].
- [10] LIGO SCIENTIFIC, VIRGO, KAGRA collaboration, Upper Limits on the Isotropic Gravitational-Wave Background from the first part of LIGO, Virgo, and KAGRA's fourth Observing Run, 2508.20721.
- [11] LISA collaboration, Laser Interferometer Space Antenna, 1702.00786.
- [12] T. Robson, N.J. Cornish and C. Liu, *The construction and use of LISA sensitivity curves*, *Class. Quant. Grav.* **36** (2019) 105011 [1803.01944].
- [13] LISA COSMOLOGY WORKING GROUP collaboration, *Cosmology with the Laser Interferometer Space Antenna*, *Living Rev. Rel.* **26** (2023) 5 [2204.05434].
- [14] W.-R. Hu and Y.-L. Wu, The Taiji Program in Space for gravitational wave physics and the nature of gravity, Natl. Sci. Rev. 4 (2017) 685.
- [15] W.-H. Ruan, Z.-K. Guo, R.-G. Cai and Y.-Z. Zhang, *Taiji program: Gravitational-wave sources*, *Int. J. Mod. Phys. A* **35** (2020) 2050075 [1807.09495].
- [16] Y.-L. Wu, Hyperunified field theory and Taiji program in space for GWD, Int. J. Mod. Phys. A 33 (2018) 1844014 [1805.10119].
- [17] TIANQIN collaboration, *TianQin: a space-borne gravitational wave detector*, *Class. Quant. Grav.* **33** (2016) 035010 [1512.02076].
- [18] TIANQIN collaboration, *The TianQin project: current progress on science and technology*, *PTEP* **2021** (2021) 05A107 [2008.10332].
- [19] J. Luo et al., The first round result from the TianQin-1 satellite, Class. Quant. Grav. 37 (2020) 185013 [2008.09534].
- [20] C. Caprini et al., Science with the space-based interferometer eLISA. II: Gravitational waves from cosmological phase transitions, JCAP **04** (2016) 001 [1512.06239].
- [21] D.J. Weir, Gravitational waves from a first order electroweak phase transition: a brief review, Phil. Trans. Roy. Soc. Lond. A 376 (2018) 20170126 [1705.01783].
- [22] A. Mazumdar and G. White, *Review of cosmic phase transitions: their significance and experimental signatures*, *Rept. Prog. Phys.* **82** (2019) 076901 [1811.01948].
- [23] C. Caprini et al., Detecting gravitational waves from cosmological phase transitions with LISA: an update, JCAP 03 (2020) 024 [1910.13125].
- [24] L. Bian et al., *The Gravitational-wave physics II: Progress, Sci. China Phys. Mech. Astron.* **64** (2021) 120401 [2106.10235].
- [25] P. Athron, C. Balázs, A. Fowlie, L. Morris and L. Wu, *Cosmological phase transitions:* From perturbative particle physics to gravitational waves, *Prog. Part. Nucl. Phys.* **135** (2024) 104094 [2305.02357].

- [26] D.E. Morrissey and M.J. Ramsey-Musolf, *Electroweak baryogenesis*, *New J. Phys.* **14** (2012) 125003 [1206.2942].
- [27] G. Boileau, N. Christensen, R. Meyer and N.J. Cornish, *Spectral separation of the stochastic gravitational-wave background for LISA: Observing both cosmological and astrophysical backgrounds*, *Phys. Rev. D* **103** (2021) 103529 [2011.05055].
- [28] G. Boileau, A. Lamberts, N.J. Cornish and R. Meyer, Spectral separation of the stochastic gravitational-wave background for LISA in the context of a modulated Galactic foreground, Mon. Not. Roy. Astron. Soc. 508 (2021) 803 [2105.04283].
- [29] M. Tinto and S.V. Dhurandhar, Time-Delay Interferometry, Living Rev. Rel. 17 (2014) 6.
- [30] T.L. Smith, T.L. Smith, R.R. Caldwell and R. Caldwell, LISA for Cosmologists: Calculating the Signal-to-Noise Ratio for Stochastic and Deterministic Sources, Phys. Rev. D 100 (2019) 104055 [1908.00546].
- [31] M.R. Adams and N.J. Cornish, *Discriminating between a Stochastic Gravitational Wave Background and Instrument Noise*, *Phys. Rev. D* **82** (2010) 022002 [1002.1291].
- [32] M. Tinto and S.V. Dhurandhar, *TIME DELAY*, *Living Rev. Rel.* **8** (2005) 4 [gr-qc/0409034].
- [33] L. Barack and C. Cutler, Confusion noise from LISA capture sources, Phys. Rev. D 70 (2004) 122002 [gr-qc/0409010].
- [34] LISA COSMOLOGY WORKING GROUP collaboration, Gravitational waves from first-order phase transitions in LISA: reconstruction pipeline and physics interpretation, JCAP 10 (2024) 020 [2403.03723].
- [35] C. Gowling and M. Hindmarsh, *Observational prospects for phase transitions at LISA:* Fisher matrix analysis, JCAP 10 (2021) 039 [2106.05984].
- [36] C. Gowling, M. Hindmarsh, D.C. Hooper and J. Torrado, *Reconstructing physical* parameters from template gravitational wave spectra at LISA: first order phase transitions, *JCAP* **04** (2023) 061 [2209.13551].
- [37] G. Boileau, N. Christensen, C. Gowling, M. Hindmarsh and R. Meyer, *Prospects for LISA to detect a gravitational-wave background from first order phase transitions*, *JCAP* **02** (2023) 056 [2209.13277].
- [38] M. Lewicki, M. Merchand, L. Sagunski, P. Schicho and D. Schmitt, *Impact of theoretical uncertainties on model parameter reconstruction from GW signals sourced by cosmological phase transitions*, *Phys. Rev. D* **110** (2024) 023538 [2403.03769].
- [39] F. Huang, Z.-C. Chen and Q.-G. Huang, Detecting Cosmological Phase Transitions with Taiji: Sensitivity Analysis and Parameter Estimation, Chin. Phys. C 49 (2025) 10 [2504.16712].
- [40] S. Guan, H.-K. Guo, D. Jiao, Q. Liang, L. Wu and Y. Zhang, *Measuring Gravitational Wave Spectrum from Electroweak Phase Transition and Higgs Self-Couplings*, 2511.00996.

- [41] G. Ashton et al., *BILBY: A user-friendly Bayesian inference library for gravitational-wave astronomy*, *Astrophys. J. Suppl.* **241** (2019) 27 [1811.02042].
- [42] M. Prathaban, D. Yallup, J. Alvey, M. Yang, W. Templeton and W. Handley, Gravitational-wave inference at GPU speed: A bilby-like nested sampling kernel within blackjax-ns, 2509.04336.
- [43] M.J. Ramsey-Musolf, *The electroweak phase transition: a collider target*, *JHEP* **09** (2020) 179 [1912.07189].
- [44] S. Di Vita, G. Durieux, C. Grojean, J. Gu, Z. Liu, G. Panico et al., *A global view on the Higgs self-coupling at lepton colliders*, *JHEP* **02** (2018) 178 [1711.03978].
- [45] ATLAS collaboration, Probing the nature of electroweak symmetry breaking with Higgs boson pairs in ATLAS, in 30th International Workshop on Deep-Inelastic Scattering and Related Subjects, 7, 2023 [2307.11467].
- [46] A. Alves, T. Ghosh, H.-K. Guo, K. Sinha and D. Vagie, *Collider and Gravitational Wave Complementarity in Exploring the Singlet Extension of the Standard Model*, *JHEP* **04** (2019) 052 [1812.09333].
- [47] H.-K. Guo, Dissipative Effects as New Observables for Cosmological Phase Transitions, 2310.10927.
- [48] V. Barger, P. Langacker, M. McCaskey, M. Ramsey-Musolf and G. Shaughnessy, *Complex Singlet Extension of the Standard Model*, *Phys. Rev. D* **79** (2009) 015018 [0811.0393].
- [49] D.K. Ghosh, D. Mukherjee, K. Mukherjee and R. Pramanick, *Complex Scalar Singlet Model: Electroweak Phase Transition and Gravitational Waves*, 2511.13426.
- [50] T. Biekötter, A. Dashko, M. Löschner and G. Weiglein, *Perturbative aspects of the electroweak phase transition with a complex singlet and implications for gravitational wave predictions*, 2511.14831.
- [51] M. Jiang, L. Bian, W. Huang and J. Shu, *Impact of a complex singlet: Electroweak baryogenesis and dark matter*, *Phys. Rev. D* **93** (2016) 065032 [1502.07574].
- [52] C.-W. Chiang, M.J. Ramsey-Musolf and E. Senaha, Standard Model with a Complex Scalar Singlet: Cosmological Implications and Theoretical Considerations, Phys. Rev. D 97 (2018) 015005 [1707.09960].
- [53] N. Chen, T. Li, Y. Wu and L. Bian, Complementarity of the future  $e^+e^-$  colliders and gravitational waves in the probe of complex singlet extension to the standard model, *Phys. Rev. D* **101** (2020) 075047 [1911.05579].
- [54] Y.B. Zeldovich, I.Y. Kobzarev and L.B. Okun, Cosmological Consequences of the Spontaneous Breakdown of Discrete Symmetry, Zh. Eksp. Teor. Fiz. 67 (1974) 3.
- [55] A. Friedland, H. Murayama and M. Perelstein, *Domain walls as dark energy*, *Phys. Rev. D* **67** (2003) 043519 [astro-ph/0205520].
- [56] S. Babak, A. Petiteau and M. Hewitson, *LISA Sensitivity and SNR Calculations*, 2108.01167.

- [57] Z.-C. Chen, Q.-G. Huang, C. Liu, L. Liu, X.-J. Liu, Y. Wu et al., *Prospects for Taiji to detect a gravitational-wave background from cosmic strings*, *JCAP* **03** (2024) 022 [2310.00411].
- [58] ATLAS collaboration, Search for triple Higgs boson production in the 6b final state using pp collisions at s=13 TeV with the ATLAS detector, Phys. Rev. D 111 (2025) 032006 [2411.02040].
- [59] ATLAS collaboration, Search for a resonance decaying into a scalar particle and a Higgs boson in the final state with two bottom quarks and two photons with 199 fb<sup>-1</sup> of data collected at  $\sqrt{s}$ =13 TeV and  $\sqrt{s}$ =13.6 TeV with the ATLAS detector, 2510.02857.